particles

MDPI

Review

Geometric Phases as Probes of Dark Sectors and Fundamental Symmetries

Antonio Capolupo [1,2,†], Gabriele Pisacane [1,2,†] and Raoul Serao [2,*,†]

[1] Department of Physics, University of Salerno, Via Giovanni Paolo II, 132, 84084 Fisciano, Italy; capolupo@sa.infn.it (A.C.); gpisacane@unisa.it (G.P.)
[2] Gruppo Collegato di Salerno, INFN, Via Giovanni Paolo II, 132, 84084 Fisciano, Italy
* Correspondence: rserao@unisa.it
† These authors contributed equally to this work.

Abstract

We review recent interferometric schemes designed to probe physics beyond the Standard Model through the detection of geometric phases. Within the kinematic approach to non-cyclic geometric phases, we discuss how interactions with hidden-sector degrees of freedom, such as axion-like particles and mirror-matter candidates, can induce potentially observable phase shifts in ordinary fermionic systems. We further show how the same geometric framework can be extended to particle mixing systems and fundamental symmetries, providing a phase-based signature of the Charge–Parity–Time (CPT) violation. These results illustrate how geometric phases can encode information that is not always directly accessible through standard transition probabilities, making quantum interferometry a complementary tool for testing dark-sector interactions, fundamental properties of elementary particles, acceleration-induced quantum-field effects, and phase-based thermometry. We also critically assess the experimental requirements and limitations of the proposed schemes.

Keywords: geometric phase; axion-like particles; mirror neutrons; CPT violation; Unruh effect; dark matter; quantum interferometry

1. Introduction

The Standard Model (SM) of particle physics describes fundamental interactions with high precision, but several observations indicate it is incomplete. Neutrino oscillations [1–16] show non-vanishing neutrino masses and flavor mixing. Precision anomalies, including the muon anomalous magnetic moment [17–19], and cosmological evidence for dark matter and dark energy [20–34] motivate searches for new particles, interactions, and deviations from fundamental symmetries.

Extensions of the SM often involve weakly coupled particles or hidden sectors. Axions and axion-like particles (ALPs) [35–41] couple feebly to ordinary matter. Mirror-matter models allow ordinary particles to mix with hidden-sector partners [42–52]. Additionally, fundamental symmetries, such as Charge–Parity–Time (CPT) invariance, can be tested in neutral particle mixing systems [53–55]. Because the expected signatures are small, high-precision quantum interferometry provides a tool to probe these weak interactions and modifications of quantum dynamics [56–60].

Geometric phases serve as robust observables in this context. Unlike dynamical phases, geometric phases—such as the Berry phase [61,62] and the non-cyclic Mukunda–Simon

Check for updates

Academic Editor: Francesco Nozzoli

Received: 5 June 2026
Revised: 2 July 2026
Accepted: 3 July 2026
Published: 8 July 2026

Copyright: © 2026 by the authors. Licensee MDPI, Basel, Switzerland. This article is an open access article distributed under the terms and conditions of the Creative Commons Attribution (CC BY) license.

phase [63]—depend on the path of a quantum state in projective Hilbert space and are gauge invariant. This framework is useful for interferometric systems where oscillations, mixing, decay, and effective interactions generate non-trivial trajectories.

This geometric approach extends to open quantum systems described by a reduced density matrix under non-unitary evolution. Here, geometric phases encode information about the coupling between a subsystem and its environment. This applies to particle mixing, dark-sector searches, quantum fields in non-inertial frames (such as the Unruh effect), and phase-based thermometry [64,65].

In this work, we review how different physical mechanisms produce anomalous geometric contributions to the phase of quantum systems. In dark-sector models, this phase arises from effective interactions or mixing with hidden states. In mixed mesons, it encodes CPT and CP violation. In open systems, it reveals acceleration or thermal effects.

The paper is organized as follows. Section 2 reviews geometric phases induced by dark-sector interactions, focusing on ALP-mediated interactions and neutron–mirror-neutron mixing. Section 3 discusses fundamental symmetries and open quantum systems, covering CPT and CP violation in mesons, acceleration-induced quantum-field effects, and quantum thermometry. Section 4 critically assesses the experimental scope and feasibility of the reviewed proposals. Section 5 contains the conclusions.

2. Geometric Phases in the Dark Sector

In this section, we review how interactions with hidden-sector degrees of freedom can affect the phase evolution of ordinary quantum systems and give rise to observable interferometric signatures. The common theoretical tool used in the examples discussed below is the kinematic formulation of the non-cyclic geometric phase [63]. For a normalized quantum state $|\psi(t)\rangle$ evolving along an open path in projective Hilbert space, the geometric phase is defined as the difference between the total phase and the dynamical phase, $\Phi^g(t) = \Phi^{\rm tot}(t) - \Phi^{\rm dyn}(t)$, where

$$\Phi^{\rm tot}(t) = \arg\langle\psi(0)|\psi(t)\rangle, \qquad \Phi^{\rm dyn}(t) = \mathrm{Im}\int_0^t \langle\psi(\tau)|\dot{\psi}(\tau)\rangle\, d\tau. \tag{1}$$

Throughout the manuscript, Re and Im denote the real and imaginary parts of a complex quantity, respectively. This definition is gauge invariant and does not require the evolution to be cyclic or adiabatic, making it suitable for interferometric systems in which the state acquires both ordinary dynamical phases and additional contributions induced by weak external interactions.

The basic idea is that dark-sector candidates can generate effective potentials or mixing terms for ordinary particles. These contributions modify the trajectory of the quantum state in Hilbert space and, consequently, the geometric phase accumulated during the evolution. In an interferometric setup, such a contribution appears as an anomalous phase shift in the interference pattern. Below, we discuss two representative examples: axion-like particles inducing effective interactions between ordinary fermions [54] and neutron–mirror-neutron mixing generated by a hidden sector [55].

2.1. Axion-like Particles

Axions and axion-like particles (ALPs) are candidates for the dark sector. Beyond their coupling to photons, ALPs can couple to fermions and mediate spin-dependent interactions between ordinary particles. In the neutron sector, this interaction modifies the phase accumulated during propagation, altering the interference pattern of a neutron interferometer.

https://doi.org/10.3390/particles9030071

The pseudoscalar interaction between the axion field φ and fermions is described by [54]

$$\mathcal{L}_{\rm INT} = -\sum_{j=1,2} i g_{aj}\, \varphi\, \bar{\psi}_j \gamma_5 \psi_j, \tag{2}$$

Here, $j = 1, 2$ labels the two fermionic fields participating in the exchange interaction, ψ_j denotes the corresponding fermion field, and g_{aj} is the dimensionless ALP–fermion coupling. For the neutron–neutron interaction considered below, both fields describe neutrons and $g_{a1} = g_{a2} = g_{aNN} \equiv g_p$.

In the nonrelativistic regime, axion exchange induces a spin-dependent interaction. For inter-neutron distances $r > 10^{-12}$ m, where short-range nuclear forces are negligible, the two-body Hamiltonian includes the magnetic dipole–dipole interaction and the ALP-mediated contribution:

$$H_{ij} = -\frac{\mathcal{A}}{r_{ij}^3}\left[\left(3 - \mathcal{B}e^{-m r_{ij}} K^{(a)}(r_{ij})\right)\sigma_i^{r_{ij}}\sigma_j^{r_{ij}} - \left(1 - \mathcal{B}e^{-m r_{ij}} K^{(b)}(r_{ij})\right)\boldsymbol{\sigma}_i \cdot \boldsymbol{\sigma}_j\right]. \tag{3}$$

Here, $\mathbf{r}_{ij} = \mathbf{r}_i - \mathbf{r}_j$ is the relative position of neutrons i and j, $r_{ij} = |\mathbf{r}_{ij}|$, and $\hat{\mathbf{r}}_{ij} = \mathbf{r}_{ij}/r_{ij}$. The vector $\boldsymbol{\sigma}_i$ denotes the Pauli spin operator of neutron i, while $\sigma_i^{r_{ij}} \equiv \boldsymbol{\sigma}_i \cdot \hat{\mathbf{r}}_{ij}$. The ALP-mediated terms follow from the nonrelativistic spin-dependent potential generated by pseudoscalar exchange, as implemented in the neutron-interferometric construction reviewed in Ref. [54]. Here $\mathcal{A} = \frac{g^2\alpha}{16M^2}$ and $\mathcal{B} = \frac{g_{aNN}^2}{\pi\alpha g^2} = \frac{g_p^2}{\pi\alpha g^2}$, where M is the neutron mass, g is the neutron g-factor, α is the fine-structure constant, and m is the ALP mass. The radial functions entering the Yukawa-suppressed spin potential are $K^{(a)}(r) = m^2r^2 + 3mr + 3$ and $K^{(b)}(r) = mr + 1$; they follow from the nonrelativistic reduction of the pseudoscalar-exchange interaction. The parameter $\mathcal{B}$ measures the relative strength of the axion-induced interaction. For $g_{aNN} = 0$, the Hamiltonian reduces to the magnetic dipole–dipole case.

Following the one-dimensional mean-field construction developed in Ref. [54], the many-neutron interaction is reduced to an effective single-particle description and encoded in an effective magnetic field. In the setup shown in Figure 1, a coherent cold-neutron beam is split into two sub-beams, I and II, with identical mean inter-neutron separation $d_I = d_{II} = d$. Within the one-dimensional beam approximation adopted in Ref. [33], d denotes the mean longitudinal separation between consecutive neutrons in the effective one-dimensional beam, rather than a three-dimensional nearest-neighbour distance. If $I_{\rm 1D}$ denotes the effective neutron rate entering this approximation and $\bar{v}$ is the mean longitudinal velocity, then $d \simeq \bar{v}/I_{\rm 1D}$. The quantity $I_{\rm 1D}$ should not be identified, without further modelling, with the total neutron rate integrated over the full beam cross section. They propagate through external magnetic fields of equal magnitude but different orientations: one polarization is parallel to the propagation direction, and the other is orthogonal.

The effective single-neutron Schrödinger equation yields a relative phase:

$$\Delta\phi(t) = [G_m(d) + G_a(d)]t, \tag{4}$$

where $G_m(d) = \frac{6\mathcal{A}}{d^3}\zeta(3)$ is the standard magnetic dipole–dipole rate, and the ALP-induced rate is

$$G_a(d) = -\frac{6\mathcal{A}\mathcal{B}}{d^3}\mathrm{Li}_3\left(e^{-md}\right) - \frac{6\mathcal{A}\mathcal{B}m}{d^2}\mathrm{Li}_2\left(e^{-md}\right) + \frac{2\mathcal{A}\mathcal{B}m^2}{d}\log\left(1 - e^{-md}\right), \tag{5}$$

with $\zeta(s)$ denoting the Riemann zeta function and $\mathrm{Li}_s(z)$ the polylogarithm.

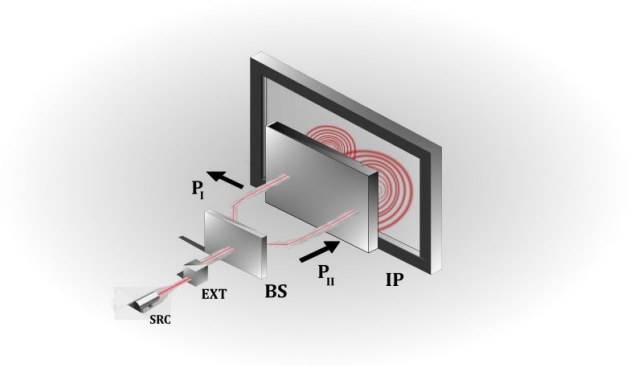


Figure 1. Schematic neutron interferometer for probing an ALP-mediated neutron–neutron interaction. The two polarized sub-beams propagate through magnetic fields of equal magnitude and different orientation.

The ALP contribution is isolated by setting the propagation time to the recurrence time:

$$T_k = \frac{k\pi d^3}{3\mathcal{A}\zeta(3)}, \qquad k \in \mathbb{Z}. \tag{6}$$

Experimentally, the recurrence condition cannot be imposed with infinite precision. Let the actual propagation time be $T = T_k + \delta T$, and let the magnetic interaction rate differ from its nominal value by δG_m. To first order, the residual ordinary magnetic phase is $\delta\phi_m \simeq 2\pi k(\delta T/T_k + \delta G_m/G_m)$. Since $G_m(d) \propto d^{-3}$, an uncertainty in the effective longitudinal separation gives $\delta G_m/G_m \simeq -3\,\delta d/d$, and therefore $\delta\phi_m \simeq 2\pi k(\delta T/T_k - 3\,\delta d/d)$. To keep this residual background below a target phase uncertainty $\delta\phi_{\text{target}}$, the combined fractional detuning must satisfy $|\delta T/T_k - 3\,\delta d/d| \lesssim \delta\phi_{\text{target}}/(2\pi k)$. For $k = 1$ and $\delta\phi_{\text{target}} = 10^{-3}$ rad, this condition requires a combined fractional precision of approximately 1.6×10^{-4}. If the uncertainty in d were negligible, this would correspond to $\delta T \lesssim 1.6\,\mu\text{s}$ for $T_1 = 9.9 \times 10^{-3}\,\text{s}$, and to $\delta T \lesssim 1.6\,\text{ms}$ for $T_1 = 9.9\,\text{s}$. In practice, the recurrence point would have to be calibrated by scanning the controllable flight time $T = L/\bar{v}$, through the path length or velocity selection, and fitting the ordinary interference fringe around an integer maximum. The residual detuning from this calibrated point must be propagated as a systematic uncertainty on the ALP-induced phase. The strong cubic dependence of the recurrence time on d is experimentally decisive. For $k = 1$ and standard neutron parameters, one finds $T_1 \simeq 9.9 \times 10^{-3}(d/10^{-9}\,\text{m})^3\,\text{s}$. Consequently, $d = 10^{-9}\,\text{m}$, $10^{-8}\,\text{m}$, and $10^{-6}\,\text{m}$ correspond approximately to $T_1 = 9.9 \times 10^{-3}\,\text{s}$, $9.9\,\text{s}$, and $9.9 \times 10^6\,\text{s}$, respectively. The last value, corresponding to approximately 115 days, is not a viable recurrence-time benchmark. The panels employing $d = 10^{-6}\,\text{m}$ are retained only to illustrate the theoretical dependence on the dimensionless quantity md and the onset of Yukawa suppression. For a representative ultracold-neutron velocity $\bar{v} \simeq 1\,\text{m}\,\text{s}^{-1}$, the separations $d = 10^{-8}\,\text{m}$ and $d = 10^{-9}\,\text{m}$ correspond to effective one-dimensional rates of order $I_{1\text{D}} \sim 10^8\,\text{s}^{-1}$ and $I_{1\text{D}} \sim 10^9\,\text{s}^{-1}$, respectively. Realizing these rates in a coherent and polarized beam would additionally require accounting for losses due to monochromatization, collimation, polarization, beam splitting, coherence selection, and propagation. Such conditions have not been demonstrated in a complete neutron-interferometric apparatus. The plotted values should therefore be interpreted as theoretical sensitivity benchmarks rather than as presently achieved experimental parameters. At this time, the magnetic phase satisfies $G_m(d)T_k = 2\pi k$ and vanishes modulo 2π. The residual phase is due to the ALP-mediated interaction:

$$\Delta\phi(T_k) = \left\{ \frac{k\pi\mathcal{B}}{3\zeta(3)} \left[2m^2d^2 \log\left(1 - e^{-md}\right) - 6md\,\text{Li}_2\left(e^{-md}\right) - 6\,\text{Li}_3\left(e^{-md}\right) \right] \right\}_{\text{mod } 2ß}. \tag{7}$$

https://doi.org/10.3390/particles9030071

This expression vanishes for $\mathcal{B} = 0$. A non-zero residual phase represents a signature of the ALP-mediated interaction.

For $md \ll 1$, where Yukawa damping is negligible, the phase reduces to

$$\Delta\phi(T_k) \simeq \{-2k\pi\mathcal{B}\}_{\mathrm{mod}\,2ß}. \tag{8}$$

Here, the phase depends primarily on the coupling $\mathcal{B} \propto g_{aNN}^2$ and is independent of the ALP mass and inter-neutron distance in the regime $md \ll 1$. This behavior is shown in Figure 2: for small md, the curves are separated by the coupling value, while the mass dependence appears when the Yukawa factor e^{-md} suppresses the interaction. Equations (4)–(8) follow from the one-dimensional mean-field construction developed in Ref. [54]. The curves in Figure 2 should not be interpreted as projected exclusion limits. They show the phase predicted when g_{aNN} is set equal to three laboratory benchmark bounds adopted in Ref. [54]: g_{CP}, derived from effective Casimir-pressure measurements; g_{CF}, derived from differential Casimir-force measurements; and g_{IE}, derived from an isoelectronic experiment. For comparison, the isoelectronic benchmark used in Ref. [54] is $g_{\mathrm{IE}} \simeq 3.6 \times 10^{-3}$ at $m = 10^{-3}$ eV, $g_{\mathrm{IE}} \simeq 6 \times 10^{-3}$ at $m = 5 \times 10^{-2}$ eV, and $g_{\mathrm{IE}} \simeq 7 \times 10^{-2}$ at $m = 1$ eV. The blue dashed curve in Figure 2 displays the phase obtained when the coupling saturates this isoelectronic benchmark. The proposed interferometric method is complementary to these existing force measurements because it probes the neutron–neutron pseudoscalar interaction directly through g_{aNN}, rather than an axion–photon coupling, and uses a phase observable in which the ordinary magnetic dipole–dipole contribution is suppressed at the recurrence point. A quantitative exclusion curve would, however, require a demonstrated phase resolution, a calibrated uncertainty in the recurrence condition, and a realistic coherent neutron rate. Since these ingredients are not presently available, Figure 2 is presented as a comparison with existing laboratory coupling benchmarks rather than as a projected exclusion region. The same behavior determines the contour plots in Figure 3. For small inter-neutron distances, the phase contours are horizontal over a wide mass range, showing that the signal is controlled by the axion–neutron coupling. At larger md, the contours bend due to Yukawa suppression. Its practical sensitivity is controlled not only by the phase resolution but also by the simultaneous requirements of high neutron rate, narrow velocity distribution, polarization, spatial coherence, accurate recurrence-point calibration, and sufficiently short recurrence time. These limitations are discussed further in Section 4.

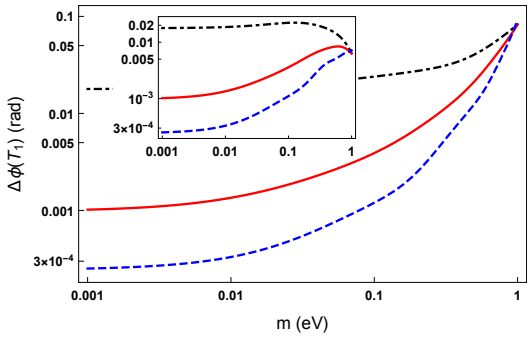


Figure 2. Residual phase $|\Delta\phi(T_1)|$ mod 2π as a function of the ALP mass. The black dot-dashed curve corresponds to the effective Casimir-pressure benchmark g_{CP}, the red solid curve to the differential Casimir-force benchmark g_{CF}, and the blue dashed curve to the isoelectronic benchmark g_{IE}, as adopted in Ref. [54]. The main panel uses $d = 10^{-8}$ m. The inset, obtained for $d = 10^{-6}$ m, is included only as an illustrative theoretical benchmark.

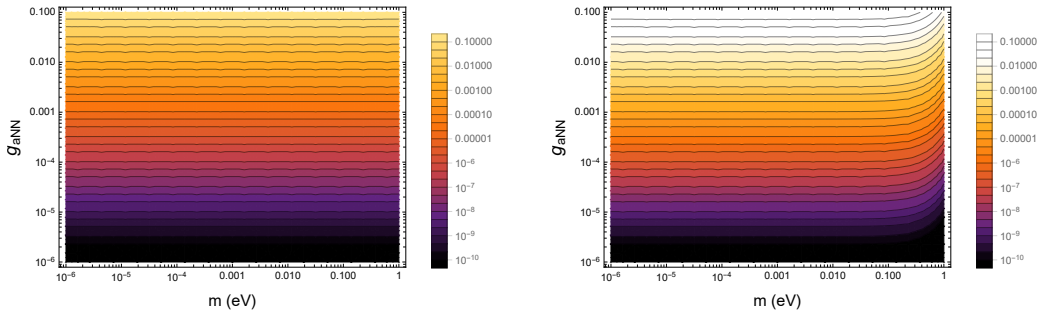


Figure 3. Contours of $|\Delta\phi(T_1)|$ mod 2π in the (m, g_{aNN}) plane for $d = 10^{-9}$ m (**left**) and $d = 10^{-6}$ m (**right**). The right panel illustrates the onset of Yukawa suppression and does not represent a viable recurrence-time benchmark.

2.2. Mirror Matter and Neutron Mixing

Mirror-matter models introduce a hidden gauge sector whose particle content and interactions reproduce, or approximately reproduce, those of the Standard Model. A mirror neutron n' is the neutral baryonic counterpart of the ordinary neutron in this hidden sector. It carries no ordinary colour or electric charge and is therefore sterile with respect to ordinary strong and electromagnetic interactions. A weak portal interaction may nevertheless generate an off-diagonal mass term and induce neutron–mirror-neutron oscillations. Such mixing provides a low-energy observable of the hidden sector that may be probed through geometric phase shifts in neutron interferometry [55]. Let $|n\rangle$ and $|n'\rangle$ denote the flavor states of the ordinary and mirror neutron. These states are related to the mass propagation eigenstates $|n_1\rangle$ and $|n_2\rangle$ by the orthogonal transformation:

$$\begin{pmatrix} |n\rangle \\ |n'\rangle \end{pmatrix} = \begin{pmatrix} \cos\theta & \sin\theta \\ -\sin\theta & \cos\theta \end{pmatrix} \begin{pmatrix} |n_1\rangle \\ |n_2\rangle \end{pmatrix}. \tag{9}$$

For a fixed spin polarization, the two-level dynamics are described by the effective Hamiltonian:

$$H = \begin{pmatrix} m_n + \Delta E & \epsilon_{nn'} \\ \epsilon_{nn'} & m_n + \delta m \end{pmatrix}, \tag{10}$$

where m_n is the neutron mass, $\epsilon_{nn'}$ is the mixing parameter, and $\delta m = m_{n'} - m_n$ is the mass splitting between the two sectors. The ΔE term accounts for energy shifts induced by external fields; for a neutron with magnetic moment μ_n aligned with a uniform magnetic field B, this shift is $\Delta E = |\mu_n B|$. Diagonalization yields the effective mixing angle,

$$\tan(2\theta) = \frac{2\epsilon_{nn'}}{\delta m - \Delta E}, \tag{11}$$

and the mass eigenvalues

$$m_{1,2} = \frac{1}{2}\left[2m_n + \Delta E + \delta m \mp \sqrt{(\Delta E - \delta m)^2 + 4\epsilon_{nn'}^2}\right]. \tag{12}$$

For a neutron with momentum k, the state frequencies are $\omega_j = \sqrt{k^2 + m_j^2}$ $(j = 1, 2)$, defining the splitting $\Delta\omega = \omega_2 - \omega_1$. Neglecting a global phase factor, the time evolution of an initial ordinary neutron state is

$$|n(t)\rangle = \cos\theta\, e^{i\frac{\Delta\omega}{2}t}\,|n_1\rangle + \sin\theta\, e^{-i\frac{\Delta\omega}{2}t}\,|n_2\rangle\,. \tag{13}$$

Using the kinematic definition for open paths, the non-cyclic geometric phase is

$$\Phi^g(t) = \arg\left[\cos\left(\frac{\Delta\omega}{2}t\right) + i\sin\left(\frac{\Delta\omega}{2}t\right)\cos(2\theta)\right] - \frac{\Delta\omega t}{2}\cos(2\theta). \tag{14}$$

This phase is gauge and reparametrization invariant. It provides a direct indicator of the mixing: in the limit $\epsilon_{nn'} \to 0$ ($\theta \to 0$), the geometric contribution vanishes. To extract this quantity experimentally, the interferometric setup must isolate the geometric phase difference. As shown in Figure 4, a polarized neutron beam is split into two sub-beams propagating along arms a and b. These arms have unequal lengths (l_a and l_b) and are subjected to co-aligned magnetic fields of different magnitudes (B_a and B_b). Upon recombination, the interference pattern depends on the net phase difference. For each arm $J \in \{a, b\}$, the magnetic field defines the parameters:

$$\theta_J = \frac{1}{2}\arctan\left(\frac{2\epsilon_{nn'}}{\delta m - |\mu_n B_J|}\right), \qquad \Delta\omega_J = \omega_2(B_J) - \omega_1(B_J). \tag{15}$$

The dynamical phase difference is canceled by tuning the asymmetry of the interferometer arms according to the condition:

$$l_b = \frac{\Delta\omega_a \cos(2\theta_a)}{\Delta\omega_b \cos(2\theta_b)}\, l_a. \tag{16}$$

Setting the propagation time $t_a = l_a/v$, where v is the neutron velocity, the residual phase is entirely geometric:

$$\begin{aligned}\Delta\Phi = \Delta\Phi^g = &\arg\left[\cos\left(\frac{\Delta\omega_a l_a}{2v}\frac{\cos(2\theta_a)}{\cos(2\theta_b)}\right) + i\sin\left(\frac{\Delta\omega_a l_a}{2v}\frac{\cos(2\theta_a)}{\cos(2\theta_b)}\right)\cos(2\theta_b)\right] \\ &- \arg\left[\cos\left(\frac{\Delta\omega_a l_a}{2v}\right) + i\sin\left(\frac{\Delta\omega_a l_a}{2v}\right)\cos(2\theta_a)\right].\end{aligned} \tag{17}$$

This phase difference is the main observable. It vanishes for uncoupled sectors and depends on the mirror parameters $\epsilon_{nn'}$ and δm, as well as on the tunable external fields and arm lengths. The dependence of the geometric phase difference on the mirror-sector parameters is shown in Figure 5. The main panel uses $\epsilon_{nn'} = 10^{-10}$ eV, 5×10^{-9} eV, and 10^{-9} eV, while the inset uses $\delta m = 10^{-8}$ eV, 5×10^{-8} eV, and 10^{-7} eV. These values reproduce the illustrative benchmarks adopted in Ref. [34] to display the dependence of the phase on the mirror-sector parameters for the chosen magnetic fields. They should not be interpreted as a global experimentally allowed region. For fixed interferometric parameters, the phase is enhanced for smaller mass splittings or larger mixing energies, particularly when the magnetic energy $|\mu_n B_J|$ approaches the mass gap δm. Ambient magnetic fields, including the Earth's field, modify the effective mixing and must therefore be controlled or included in the analysis. A single phase measurement cannot determine both $\epsilon_{nn'}$ and δm independently; measurements at different magnetic fields or arm lengths would be required to break this degeneracy. The values shown in Figure 5 are illustrative benchmarks inherited from Ref. [55] and should not be interpreted as a currently allowed parameter region. Dedicated disappearance and regeneration searches constrain combinations of the mass splitting, mixing energy, and ordinary or mirror magnetic fields. A recent regeneration search reported no excess above background and improved the limits on neutron–sterile-neutron transformations for mass splittings between approximately 0.1 and 1000 neV. The translation of these bounds into the $(\epsilon_{nn'}, \delta m)$ plane employed here depends on the assumed ordinary and mirror magnetic fields.

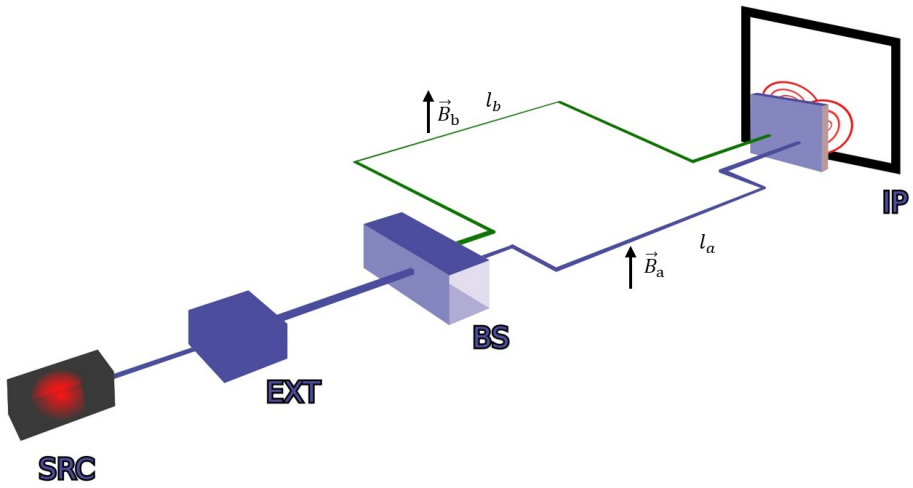


Figure 4. Asymmetric neutron interferometer proposed to probe neutron–mirror-neutron mixing. The two arms have unequal lengths l_a and l_b and are subjected to magnetic fields B_a and B_b. The parameters are adjusted according to the dynamical-phase cancellation condition in Equation (16).

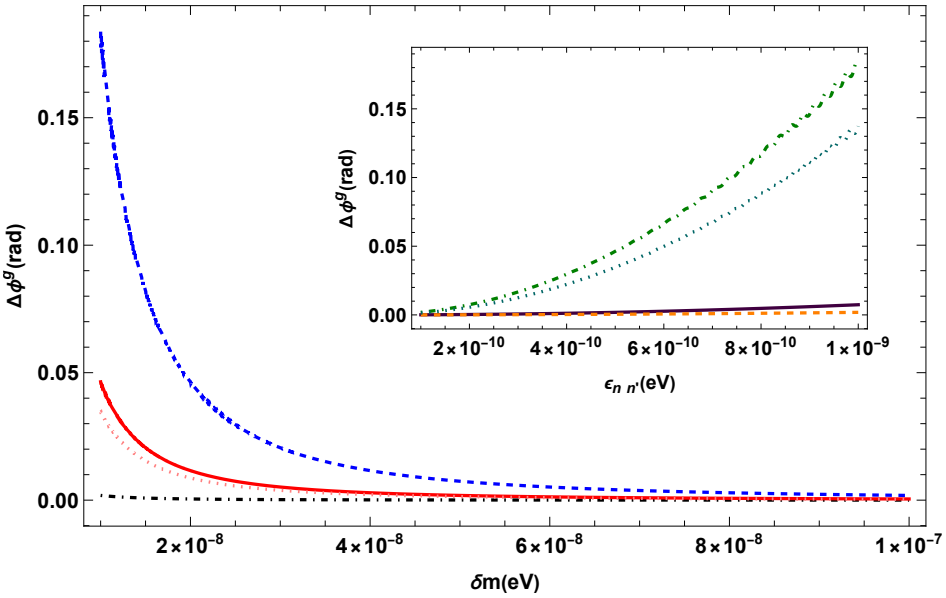


Figure 5. Geometric phase difference $\Delta\phi^g$ versus the mass splitting δm for mixing strengths: $\epsilon_{nn'} = 10^{-10}$ eV (black dotted), $\epsilon_{nn'} = 5 \times 10^{-9}$ eV (red solid), and $\epsilon_{nn'} = 10^{-9}$ eV (blue dashed). The inset shows the scaling with $\epsilon_{nn'}$ at fixed mass gaps: $\delta m = 10^{-8}$ eV (green dotted), 5×10^{-8} eV (purple solid), and 10^{-7} eV (orange dashed). Setup parameters are $\lambda = 10$ Å, $B_a = 0$ T, $B_b = 2 \times 10^{-4}$ T, and $l_a = 20$ cm. The pink and cyan dotted lines show the effect of the Earth's magnetic field ($B_a = 5 \times 10^{-5}$ T).

3. Probing Fundamental Symmetries and Particle Nature

The geometric-phase framework is not limited to phase shifts induced by external interactions or dark-sector potentials. It can also be applied to systems in which the relevant physical information is encoded in the internal structure of the Hamiltonian, as happens in particle mixing, oscillations, and symmetry-violating dynamics. In these cases, the geometric phase does not simply measure the effect of an additional interaction, but rather probes how the quantum state evolves in the space of physical configurations. This observation makes geometric phases particularly useful for investigating fundamental symmetries and intrinsic particle properties. In neutral meson systems, for instance, possible violations of Charge–Parity–Time (CPT) symmetry modify the effective non-

Hermitian Hamiltonian governing particle–antiparticle oscillations. Such modifications can generate different geometric phases for a particle and its antiparticle, providing a phase-based signature of CPT violation [53].

In the following subsection, we review the role of geometric phases in probing CPT violation in mixed meson systems.

3.1. Meson Mixing, CP and CPT Violations, and Geometric Phase

Neutral meson systems provide a natural arena in which geometric phases can be used to probe fundamental discrete symmetries. Systems such as K^0–$\bar{K}^0$, B_d^0–$\bar{B}_d^0$, B_s^0–$\bar{B}_s^0$ and D^0–$\bar{D}^0$ exhibit particle–antiparticle oscillations and decay. Their effective time evolution is therefore described by a non-Hermitian Hamiltonian, and the usual Hermitian spectral decomposition has to be replaced by a biorthonormal formulation.

In the subspace spanned by the flavor states $|M^0\rangle$ and $|\bar{M}^0\rangle$, the state vector can be written as $|\psi(t)\rangle = \psi_{M^0}(t)\,|M^0\rangle + \psi_{\bar{M}^0}(t)\,|\bar{M}^0\rangle + \sum_n d_n(t)\,|n\rangle$, where $|n\rangle$ denotes the decay products. Restricting the dynamics to the $\{M^0, \bar{M}^0\}$ sector, one obtains $i\frac{d}{dt}\Psi(t) = \mathcal{H}\Psi(t)$, with $\Psi(t) = \begin{pmatrix} \psi_{M^0}(t) \\ \psi_{\bar{M}^0}(t) \end{pmatrix}$, and $\mathcal{H} = M - i\frac{\Gamma}{2} = \begin{pmatrix} \mathcal{H}_{11} & \mathcal{H}_{12} \\ \mathcal{H}_{21} & \mathcal{H}_{22} \end{pmatrix}$. Here M and Γ are Hermitian matrices. The matrix elements of $\mathcal{H}$ encode the violation or conservation of discrete symmetries. In particular, CPT invariance requires $\mathcal{H}_{11} = \mathcal{H}_{22}$, while T invariance imposes $|\mathcal{H}_{12}| = |\mathcal{H}_{21}|$. CP invariance requires both conditions to hold simultaneously.

Since $\mathcal{H}$ is in general non-Hermitian and non-normal, its right and left eigenvectors are independent. We denote by $\lambda_j = m_j - i\frac{\Gamma_j}{2}, j = L, H$, the eigenvalues of $\mathcal{H}$, where L and H indicate the light and heavy states. The right eigenvectors satisfy $\mathcal{H}\,|M_j\rangle = \lambda_j\,|M_j\rangle$, whereas the eigenvectors of the adjoint Hamiltonian satisfy $\mathcal{H}^\dagger\,|\widetilde{M}_j\rangle = \lambda_j^*\,|\widetilde{M}_j\rangle$. The appropriate basis is therefore the biorthonormal set $\{|M_j\rangle, \langle\widetilde{M}_j|\}$, obeying $\langle\widetilde{M}_i|M_j\rangle = \delta_{ij}, \sum_{j=L,H}|M_j\rangle\langle\widetilde{M}_j| = \mathbb{I}$.

It is useful to introduce the CP-violating parameter $\epsilon_{\rm CP} = \frac{|p/q|-|q/p|}{|p/q|+|q/p|} = \frac{|\mathcal{H}_{12}|-|\mathcal{H}_{21}|}{|\mathcal{H}_{12}|+|\mathcal{H}_{21}|}$, with $\frac{q}{p} = \sqrt{\frac{\mathcal{H}_{21}}{\mathcal{H}_{12}}}$, and the CPT-violating parameter $z = \frac{\mathcal{H}_{22}-\mathcal{H}_{11}}{\lambda_L-\lambda_H}$. Exact CPT invariance corresponds to $z = 0$. In terms of the eigenstates of the effective Hamiltonian, the time-evolved flavor states can be written as

$$|M^0(t)\rangle = \frac{1}{2p}\left[\sqrt{1-z}\,|M_L\rangle\,e^{-i\lambda_L t} + \sqrt{1+z}\,|M_H\rangle\,e^{-i\lambda_H t}\right], \tag{18}$$

$$|\bar{M}^0(t)\rangle = \frac{1}{2q}\left[\sqrt{1+z}\,|M_L\rangle\,e^{-i\lambda_L t} - \sqrt{1-z}\,|M_H\rangle\,e^{-i\lambda_H t}\right]. \tag{19}$$

The corresponding dual states in the biorthonormal formalism are

$$\langle\widetilde{M}^0(t)| = p\left[\sqrt{1-z}\,\langle\widetilde{M}_L|\,e^{i\lambda_L t} + \sqrt{1+z}\,\langle\widetilde{M}_H|\,e^{i\lambda_H t}\right], \tag{20}$$

$$\langle\widetilde{\bar{M}}^0(t)| = q\left[\sqrt{1+z}\,\langle\widetilde{M}_L|\,e^{i\lambda_L t} - \sqrt{1-z}\,\langle\widetilde{M}_H|\,e^{i\lambda_H t}\right]. \tag{21}$$

For a diagonalizable non-Hermitian Hamiltonian, the geometric phase can be defined by extending the Mukunda–Simon construction to the biorthonormal basis. For a state $|\psi_{\rm NH}(t)\rangle$ and its corresponding dual $\langle\widetilde{\psi}_{\rm NH}(t)|$, one has

$$\Phi_{\rm NH}(t) = \arg\langle\widetilde{\psi}_{\rm NH}(0)|\psi_{\rm NH}(t)\rangle - {\rm Im}\int_0^t \langle\widetilde{\psi}_{\rm NH}(t')|\dot{\psi}_{\rm NH}(t')\rangle\,dt'. \tag{22}$$

This phase is invariant under reparametrizations of the path and under the appropriate complex gauge transformations. For mixed mesons, four geometric phases can be introduced:

$$\Phi_{M^0M^0}(t) = \arg\langle\widetilde{M}^0(0)|M^0(t)\rangle - \mathrm{Im}\int_0^t \langle\widetilde{M}^0(t')|\dot{M}^0(t')\rangle\, dt', \tag{23}$$

$$\Phi_{\bar{M}^0\bar{M}^0}(t) = \arg\langle\widetilde{\bar{M}}^0(0)|\bar{M}^0(t)\rangle - \mathrm{Im}\int_0^t \langle\widetilde{\bar{M}}^0(t')|\dot{\bar{M}}^0(t')\rangle\, dt', \tag{24}$$

$$\Phi_{M^0\bar{M}^0}(t) = \arg\langle\widetilde{M}^0(0)|\bar{M}^0(t)\rangle - \mathrm{Im}\int_0^t \langle\widetilde{M}^0(t')|\dot{\bar{M}}^0(t')\rangle\, dt', \tag{25}$$

$$\Phi_{\bar{M}^0M^0}(t) = \arg\langle\widetilde{\bar{M}}^0(0)|M^0(t)\rangle - \mathrm{Im}\int_0^t \langle\widetilde{\bar{M}}^0(t')|\dot{M}^0(t')\rangle\, dt'. \tag{26}$$

The first two phases describe the geometric phases associated with the survival of a meson and its antiparticle. They are sensitive to the CPT-violating parameter z. The last two phases describe particle–antiparticle transitions and are instead related to CP violation. Let $\Delta m = m_H - m_L, \Delta\Gamma = \Gamma_H - \Gamma_L$. In the regime $\frac{\Delta\Gamma\, t}{2} \ll 1$, which is appropriate for the time intervals commonly used in neutral B-meson analyses, the survival phases reduce to

$$\Phi_{M^0M^0}(t) \simeq \arg\left[\cos\left(\frac{\Delta m\, t}{2}\right) + (\mathrm{Im}\, z - i\,\mathrm{Re}\, z)\sin\left(\frac{\Delta m\, t}{2}\right)\right] + \frac{t}{2}\left(\Delta m\ \mathrm{Re}\, z + \frac{\Delta\Gamma}{2}\ \mathrm{Im}\, z\right), \tag{27}$$

$$\Phi_{\bar{M}^0\bar{M}^0}(t) \simeq \arg\left[\cos\left(\frac{\Delta m\, t}{2}\right) - (\mathrm{Im}\, z - i\,\mathrm{Re}\, z)\sin\left(\frac{\Delta m\, t}{2}\right)\right] - \frac{t}{2}\left(\Delta m\ \mathrm{Re}\, z + \frac{\Delta\Gamma}{2}\ \mathrm{Im}\, z\right). \tag{28}$$

Their difference, $\Delta\Phi(t) = \Phi_{M^0M^0}(t) - \Phi_{\bar{M}^0\bar{M}^0}(t)$, is entirely controlled by the CPT-violating parameter z. In the CPT-conserving limit, $z = 0$, the two phases become equal,

$$\Phi^{\mathrm{CPT}}_{M^0M^0}(t) = \Phi^{\mathrm{CPT}}_{\bar{M}^0\bar{M}^0}(t) = \arg\left[\cos\left(\frac{\Delta m\, t}{2}\right)\right], \tag{29}$$

and therefore $\Delta\Phi(t) = 0$. A non-zero value of $\Delta\Phi(t)$ is thus a direct phase-based signature of CPT violation.

The transition phases are instead sensitive to CP violation. Keeping only the leading terms in z and working again in the regime $\Delta\Gamma\, t/2 \ll 1$, one finds

$$\Phi_{M^0\bar{M}^0}(t) \simeq \frac{\pi}{2} - \frac{m\, t}{2} + \arg\left[\frac{p}{q}\sin\left(\frac{\Delta m\, t}{2}\right)\right] - \frac{\Delta m\, t}{2}\,\mathrm{Re}\left(\frac{p}{q}\right) - \frac{\Delta\Gamma\, t}{2}\,\mathrm{Im}\left(\frac{p}{q}\right), \tag{30}$$

$$\Phi_{\bar{M}^0M^0}(t) \simeq \frac{\pi}{2} - \frac{m\, t}{2} + \arg\left[\frac{q}{p}\sin\left(\frac{\Delta m\, t}{2}\right)\right] - \frac{\Delta m\, t}{2}\,\mathrm{Re}\left(\frac{q}{p}\right) - \frac{\Delta\Gamma\, t}{2}\,\mathrm{Im}\left(\frac{q}{p}\right), \tag{31}$$

where $m = m_L + m_H$. These phases depend on the ratio q/p, and therefore on the CP-violating structure of the effective Hamiltonian. In the CP-conserving case, one has $p = q$ up to an irrelevant phase, and the two transition phases coincide:

$$\Phi^{\mathrm{CP}}_{M^0\bar{M}^0}(t) = \Phi^{\mathrm{CP}}_{\bar{M}^0M^0}(t) = \frac{\pi}{2} - \frac{(m + \Delta m)t}{2} + \arg\left[\sin\left(\frac{\Delta m\, t}{2}\right)\right]. \tag{32}$$

Thus, geometric phases provide a compact way to encode both CPT-sensitive survival effects and CP-sensitive transition effects in neutral meson systems.

For the B_s^0–$\bar{B}_s^0$ system, the CPT-sensitive phase difference $\Delta\Phi$ can be studied numerically as a function of time. This system is particularly suitable because several oscillations occur within the meson lifetime. Using the experimental parameters $m_s = 1.63007 \times 10^{13}\,\mathrm{ps}^{-1}$, $\Delta m_s = 17.77\,\mathrm{ps}^{-1}$, $\Gamma_s = 0.678\,\mathrm{ps}^{-1}$, and $\Delta\Gamma_s = -0.062\,\mathrm{ps}^{-1}$, we consider $\mathrm{Re}\, z, \mathrm{Im}\, z \in [-0.1, 0.1]$. Over this range, the phase difference depends only weakly on $\mathrm{Im}\, z$. Accordingly, in Figure 6 we set $\mathrm{Im}\, z = 0$ and show the time dependence

of $\Delta\Phi$ for different values of $\mathrm{Re}\, z$. A non-zero phase difference arises only for $z \neq 0$, namely when CPT symmetry is broken. It is important to clarify the experimental content of this construction. The geometric-phase formulation does not introduce an additional independent parameter beyond the conventional mixing quantities z and q/p, and it does not replace standard time-dependent oscillation or decay-rate analyses. Rather, it reorganizes the same complex time-dependent amplitudes into rephasing-invariant phase observables. In particular, $\Delta\Phi(t)$ provides a compact null test: it vanishes identically when $z = 0$, whereas a non-zero value tracks the CPT-violating part of the particle–antiparticle evolution. Experimentally, this phase would not be measured by inserting the meson system into a spatial interferometer. It would have to be reconstructed from the complex time-dependent amplitudes obtained in flavour-tagged decay analyses. Its potential value is therefore complementary: the specific time-dependent combination entering $\Delta\Phi(t)$ supplies a consistency observable that can be compared with conventional fits of $\mathrm{Re}\, z$, $\mathrm{Im}\, z$, and q/p. We do not claim an intrinsically superior statistical sensitivity; establishing such an advantage would require a dedicated detector-level analysis.

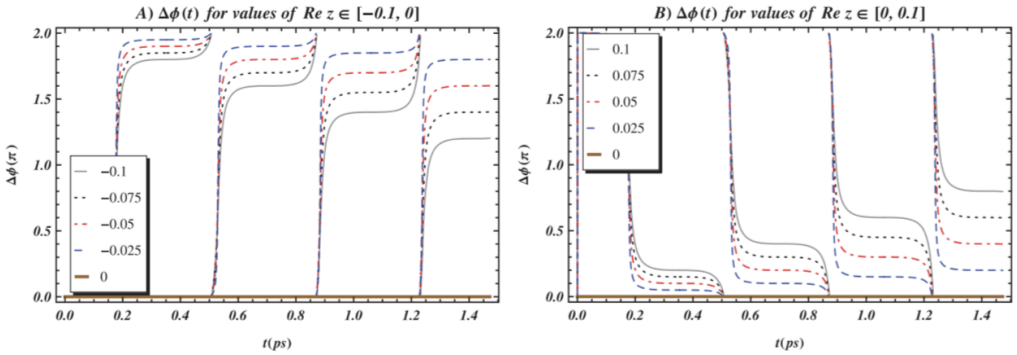


Figure 6. Phase difference $\Delta\Phi = \Phi_{B_s^0 B_s^0} - \Phi_{\bar{B}_s^0 \bar{B}_s^0}$ as a function of time for $\mathrm{Im}\, z = 0$ and different values of $\mathrm{Re}\, z$. Panel A corresponds to $\mathrm{Re}\, z \in [-0.1, 0]$ and panel B to $\mathrm{Re}\, z \in [0, 0.1]$.

3.2. Unruh Effect, Quantum Thermometry and Geometric Phase

The geometric phase can also be used to characterize systems whose evolution is non-unitary. This situation naturally arises in quantum open systems, where the degrees of freedom of interest are coupled to an external environment and the state of the subsystem is described by a reduced density matrix. In this setting, geometric phases provide a useful tool to investigate effects associated with quantum fields in non-inertial frames, including the response of a uniformly accelerated detector to the Minkowski vacuum, and can also be used to formulate interferometric schemes for precision thermometry [64,65].

For a mixed state undergoing non-unitary and non-cyclic evolution, the geometric phase can be defined in terms of the instantaneous spectral decomposition of the density matrix. Let $\rho(t) = \sum_{k=1}^{N} \lambda_k(t) \left|\varphi_k(t)\right\rangle \left\langle\varphi_k(t)\right|$, where $\lambda_k(t)$ and $\left|\varphi_k(t)\right\rangle$ are, respectively, the eigenvalues and eigenvectors of $\rho(t)$. The geometric phase is then

$$\Phi_g(t) = \sum_{k=1}^{N} \arg\left[\sqrt{\lambda_k(0)\lambda_k(t)}\, \langle\varphi_k(0)|\varphi_k(t)\rangle\right] - \mathrm{Im} \sum_{k=1}^{N} \int_0^t \lambda_k(t') \langle\varphi_k(t')|\dot{\varphi}_k(t')\rangle\, dt'. \quad (33)$$

The first term corresponds to the total phase contribution, while the second term subtracts the dynamical part.

For a two-level open system, the density matrix can be represented through the Bloch vector. Defining $n_1 = \rho_{12} + \rho_{21}$, $n_2 = i(\rho_{12} - \rho_{21})$, $n_3 = \rho_{11} - \rho_{22}$, and $r(t) =$

$\sqrt{n_1^2+n_2^2+n_3^2}$, one introduces the angles $\theta(t)=\cos^{-1}\left(\frac{n_3}{r}\right)$, and $\varphi(t)=\tan^{-1}\left(\frac{n_2}{n_1}\right)$. The eigenvectors of $\rho(t)$ may then be written as

$$|\varphi_1(t)\rangle=\begin{pmatrix}\cos\frac{\theta(t)}{2}\\ e^{i\varphi(t)}\sin\frac{\theta(t)}{2}\end{pmatrix},\qquad |\varphi_2(t)\rangle=\begin{pmatrix}\sin\frac{\theta(t)}{2}\\ -e^{i\varphi(t)}\cos\frac{\theta(t)}{2}\end{pmatrix}, \tag{34}$$

with the eigenvalues $\lambda_1(t)=\frac{1+r(t)}{2}$ and $\lambda_2(t)=\frac{1-r(t)}{2}$.

The physical system considered here is a two-level atom weakly coupled to the electromagnetic field. Its Hamiltonian can be written as

$$H=\frac{\omega_0}{2}\sigma_3+H_F-\sum_{m,n}\boldsymbol{\mu}_{mn}\cdot\mathbf{E}[x(\tau)]\,\sigma_{mn}. \tag{35}$$

Here m and n label the internal atomic energy eigenstates, ω_0 is the unperturbed atomic transition frequency, and H_F is the Hamiltonian of the quantized electromagnetic field. The operator $\sigma_{mn}=|m\rangle\langle n|$ induces the corresponding atomic transition, while $\boldsymbol{\mu}_{mn}=\langle m|\boldsymbol{\mu}|n\rangle$ is the associated electric-dipole matrix element. The operator $\mathbf{E}[x(\tau)]$ is the quantized electric field evaluated along the atomic worldline $x(\tau)$. In the weak-coupling regime, the reduced density matrix of the atom obeys a Markovian master equation of Gorini–Kossakowski–Sudarshan–Lindblad form,

$$\frac{\partial\rho(\tau)}{\partial\tau}=-i[H_{\rm eff},\rho(\tau)]+\frac{1}{2}\sum_{i,j=1}^{3}a_{ij}\left(2\sigma_j\rho\sigma_i-\sigma_i\sigma_j\rho-\rho\sigma_i\sigma_j\right), \tag{36}$$

where τ is the proper time, $H_{\rm eff}$ is the effective Hamiltonian, and a_{ij} are the coefficients of the Kossakowski matrix. The effective Hamiltonian may be written as $H_{\rm eff}=\Omega\sigma_3/2$, where Ω is the field-renormalized atomic transition frequency, including the Lamb-shift contribution. When the Lamb-shift correction is neglected, one has $\Omega\simeq\omega_0$. The coefficients a_{ij} are determined by the Fourier transform of the field correlation functions evaluated along the atomic trajectory and can be written as $a_{ij}=\Sigma\,\delta_{ij}-i\Upsilon\,\epsilon_{ijk}\delta_{k3}-\Sigma\,\delta_{i3}\delta_{j3}$, with $\Sigma=\frac{1}{4}[G(\omega_0)+G(-\omega_0)]$, $\Upsilon=\frac{1}{4}[G(\omega_0)-G(-\omega_0)]$. Here $G(\omega)$ denotes the Fourier transform of the electromagnetic two-point correlation function along the trajectory. For an initial atomic state $|\psi(0)\rangle=\cos\frac{\theta}{2}\,|+\rangle+\sin\frac{\theta}{2}\,|-\rangle$, the reduced density matrix can be written as

$$\rho(\tau)=\frac{1}{2}\begin{pmatrix}1+\chi(\tau) & e^{-i\Omega\tau}\sqrt{\xi^2(\tau)-\chi^2(\tau)}\\ e^{i\Omega\tau}\sqrt{\xi^2(\tau)-\chi^2(\tau)} & 1-\chi(\tau)\end{pmatrix}, \tag{37}$$

where $\xi(\tau)=\sqrt{\chi^2(\tau)+e^{-4\Sigma\tau}\sin^2\theta}$ and $\chi(\tau)=e^{-4\Sigma\tau}\cos\theta+\frac{\Upsilon}{\Sigma}\left(e^{-4\Sigma\tau}-1\right)$. The eigenvalues are $\lambda_\pm(\tau)=\frac{1\pm\xi(\tau)}{2}$, and the corresponding eigenvectors can be chosen as

$$|\phi_+(\tau)\rangle=\cos\frac{\theta(\tau)}{2}\,|+\rangle+\sin\frac{\theta(\tau)}{2}e^{i\Omega\tau}\,|-\rangle\,, \tag{38}$$

$$|\phi_-(\tau)\rangle=\sin\frac{\theta(\tau)}{2}\,|+\rangle-\cos\frac{\theta(\tau)}{2}e^{i\Omega\tau}\,|-\rangle\,. \tag{39}$$

Substituting these expressions into the mixed-state definition gives

$$\Phi_g(t)=\arg\left[\cos\frac{\theta}{2}\cos\frac{\theta(t)}{2}+\sin\frac{\theta}{2}\sin\frac{\theta(t)}{2}e^{i\Omega t}\right]-\frac{\Omega}{2}\int_0^t[1-\xi(\tau)\cos\theta(\tau)]d\tau. \tag{40}$$

To study acceleration-induced quantum-field effects, we compare two identical atomic detectors weakly coupled to the quantized electromagnetic field. One detector follows a uniformly accelerated trajectory, while the other remains inertial. This comparison is

not purely kinematic: the coefficients of the reduced master equation are determined by the electromagnetic vacuum two-point correlation function evaluated along the respective worldlines. For uniform acceleration along the x direction, the trajectory is

$$x(\tau) = \frac{c^2}{a}\cosh\left(\frac{a\tau}{c}\right), \qquad t(\tau) = \frac{c}{a}\sinh\left(\frac{a\tau}{c}\right), \tag{41}$$

where a is the proper acceleration. The coefficients entering the master equation become $\Sigma_a = \frac{\gamma_0}{4}\left(1+\frac{a^2}{c^2\omega_0^2}\right)\frac{e^{2\pi c\omega_0/a}+1}{e^{2\pi c\omega_0/a}-1}$ and $\Upsilon_a = \frac{\gamma_0}{4}\left(1+\frac{a^2}{c^2\omega_0^2}\right)$, where γ_0 is the spontaneous emission rate. In the inertial limit one has $\Sigma_{a=0} = \Upsilon_{a=0} = \frac{\gamma_0}{4}$. The factor $[\exp(2\pi c\omega_0/a)-1]^{-1}$ is the Bose–Einstein factor associated with the Unruh temperature $T_U = \hbar a/(2\pi c k_B)$. It originates from the Fourier transform of the Minkowski-vacuum electromagnetic two-point correlation function evaluated along the uniformly accelerated trajectory. The acceleration-dependent correction is therefore generated by the atom–field interaction and cannot be reduced to a transformation of coordinates or proper time. For the electromagnetic field, however, the additional factor $1 + a^2/(c^2\omega_0^2)$ also modifies the detector spectral response. The resulting phase difference should consequently be interpreted as an acceleration-induced quantum-field vacuum response containing an Unruh-related thermal contribution, rather than as an experimentally unique or model-independent proof of the Unruh effect.

We define the acceleration-induced geometric-phase difference as

$$\Delta\Phi_a(t) = \Phi_a(t) - \Phi_{a=0}(t), \tag{42}$$

where $\Phi_a(t)$ and $\Phi_{a=0}(t)$ are the geometric phases acquired by the accelerated and inertial detectors, respectively. This difference probes the modification of the quantum-field vacuum response sampled along the accelerated trajectory and contains the thermal contribution associated with the Unruh effect. It should not, by itself, be interpreted as an experimentally unique observation of the Unruh effect, since acceleration-induced level shifts, the external mechanism producing the trajectory, trajectory imperfections, and residual interferometric phases must also be controlled. In an interferometric realization, the relative dynamical phase may be suppressed by an appropriate choice of the arm lengths.

The size of the effect depends strongly on the atomic transition used. Hyperfine transitions with small frequencies and suitable spontaneous-emission rates enhance the ratio γ_0/ω_0. In the main panel of Figure 7, the gray dot-dashed curve refers to the ^{87}Rb $5^2P_{1/2}$, $F = 1 \to 2$ transition, with $\omega_0 = 814.5\,\mathrm{MHz}$ and $\gamma_0 = 36.129\,\mathrm{MHz}$, while the green solid curve refers to the ^{133}Cs $6^2P_{1/2}$, $F = 3 \to 4$ transition, with $\omega_0 = 1167.68\,\mathrm{MHz}$ and $\gamma_0 = 28.743\,\mathrm{MHz}$. In the inset, the blue dashed curve refers to the ^{85}Rb $5^2S_{1/2}$, $F = 1 \to 2$ transition, with $\omega_0 = 3.035\,\mathrm{GHz}$, and the red dot-dashed curve to the ^{87}Rb $5^2S_{1/2}$, $F = 1 \to 2$ transition, with $\omega_0 = 6.843\,\mathrm{GHz}$. The displayed decay rate for the two inset curves corresponds to the D_1 transition, $\gamma_0 = 36.129\,\mathrm{MHz}$ [65]. The main-panel transitions yield phase differences of order $10^{-4}\pi$ for accelerations of order $10^{16}\,\mathrm{m\,s^{-2}}$, whereas the inset transitions require accelerations of order $10^{17}\,\mathrm{m\,s^{-2}}$. The evolution times are chosen of order $1/\omega_0$, so that spontaneous emission remains negligible and the atom can be treated as quasi-stable.

The atomic trajectory is prescribed externally in the detector model, and the physical mechanism producing the acceleration is not included in the Hamiltonian. This distinction is essential when assessing the experimental feasibility of the proposal. For a ^{87}Rb atom undergoing an acceleration $a \sim 10^{16}\,\mathrm{m\,s^{-2}}$, the required force is of order $10^{-9}\,\mathrm{N}$. As an order-of-magnitude comparison, a hypothetical particle carrying one elementary charge and subjected to the same force would require an electric field of order $10^{10}\,\mathrm{V\,m^{-1}}$. A neutral atom would instead require extreme electric, magnetic, or optical-field gradients.

Such fields could produce substantial Stark or Zeeman shifts, deform the atomic levels, invalidate the assumed fixed hyperfine two-level description, or ionize the atom. In the formal calculation, a is the proper acceleration of the atomic centre-of-mass worldline in Equation (41), rather than an acceleration generated merely by changing coordinates. An interferometric interpretation would therefore compare an inertial branch with a branch whose atomic wavepacket follows the prescribed uniformly accelerated worldline. The present model does not specify a physical mechanism capable of applying this acceleration selectively to one interferometer arm while simultaneously preserving the internal two-level structure, path coherence, and recombination conditions. We therefore do not claim that such a differential atom interferometer is presently realizable. An effective or analogue simulation of acceleration would constitute a different proposal. To reproduce the detector response calculated here, the simulated environment would have to generate the same field correlation function sampled along the accelerated Minkowski worldline. No such mapping is constructed in the present review. The numerical results should consequently be interpreted as predictions of an idealized physically accelerated-detector model, and not as a demonstrated real-atom or simulated-acceleration protocol.

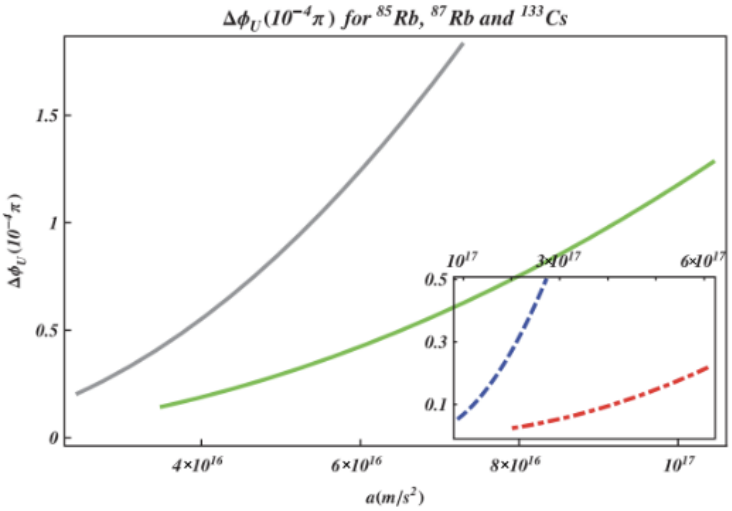


Figure 7. Acceleration-induced geometric-phase difference $\Delta\Phi_a$ as a function of the proper acceleration a, for evolution times of order $t \simeq 1/\omega_0$. In the main panel, the gray curve corresponds to the ^{87}Rb $5^2P_{1/2}$, $F = 1 \to 2$ transition, while the green solid curve corresponds to the ^{133}Cs $6^2P_{1/2}$, $F = 3 \to 4$ transition. In the inset, the blue dashed curve corresponds to the ^{85}Rb $5^2S_{1/2}$, $F = 1 \to 2$ transition, while the red dot-dashed curve corresponds to the ^{87}Rb $5^2S_{1/2}$, $F = 1 \to 2$ transition. The atomic parameters are specified in the main text.

The same open-system geometric phase can be used for thermometry. If an atom interacts with a thermal state at temperature T, the coefficients Σ and Υ become temperature dependent. Denoting them by Σ_T and Υ_T, one has $\Upsilon_T = \frac{\gamma_0}{4}\left(1 + \frac{4\pi^2 k_B^2 T^2}{\omega_0^2}\right)$, and $\Sigma_T = \frac{\gamma_0}{4}\left(1 + \frac{4\pi^2 k_B^2 T^2}{\omega_0^2}\right)\frac{e^{\omega_0/k_B T}+1}{e^{\omega_0/k_B T}-1}$. The geometric phase acquired by the atom therefore depends on the temperature of the thermal environment.

A phase-based thermometer can be designed by letting two atoms, or two branches of the same interferometric setup, interact with thermal reservoirs at different temperatures. If the temperature T_h of one reservoir is known, the temperature T_c of the other can be inferred from the measured phase difference $\Delta\Phi_T(t) = \Phi_{T_h}(t) - \Phi_{T_c}(t)$. For suitable hyperfine transitions, the phase difference remains appreciable even when the colder source has a temperature much smaller than the reference one. This behavior is illustrated in Figure 8, where $\Delta\Phi_T$ is shown as a function of the cold-source temperature for different

atomic transitions and reference temperatures. Thus, the geometric phase provides a possible interferometric route both to probing acceleration-induced thermal effects and to performing high-precision temperature measurements.

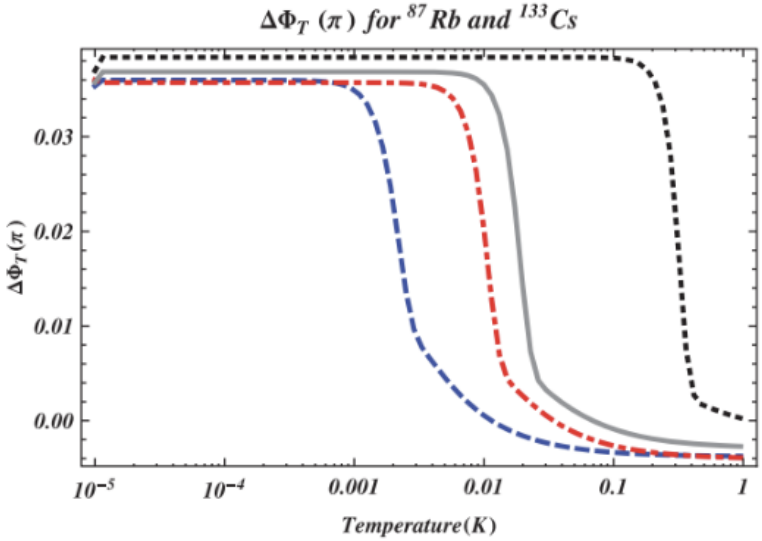


Figure 8. Geometric-phase difference $\Delta\Phi_T$ as a function of the cold-source temperature T_c. The blue dashed curve corresponds to the ^{133}Cs $6^2P_{3/2}$, $F = 4 \to 5$ transition with $T_h = 10^{-2}$ K. The red dot-dashed curve corresponds to the ^{87}Rb $5^2P_{1/2}$, $F = 1 \to 2$ transition with $T_h = 3 \times 10^{-2}$ K. The gray solid curve corresponds to the ^{133}Cs $6^2P_{1/2}$, $F = 3 \to 4$ transition with $T_h = 6 \times 10^{-2}$ K. The black dotted curve corresponds to the ^{133}Cs $6^2S_{1/2}$, $F = 3 \to 4$ transition with $T_h = 1$ K. The evolution time is $t \simeq 1/(4\omega_0)$.

4. Experimental Scope and Feasibility

The proposals reviewed in this article have markedly different degrees of experimental maturity. Their common purpose is to identify geometric-phase observables sensitive to weak interactions, hidden-sector mixing, symmetry violation, or environmental effects. Several numerical examples, however, should be interpreted as theoretical sensitivity studies rather than as specifications of presently available experiments.

For the ALP-mediated neutron scheme, the relevant benchmarks are $d = 10^{-9}$ m, 10^{-8} m, and 10^{-6} m, corresponding to recurrence times $T_1 \simeq 9.9 \times 10^{-3}$ s, 9.9 s, and 9.9×10^6 s, respectively. For $\bar{v} \simeq 1\,\mathrm{m\,s^{-1}}$, the first two separations correspond to effective one-dimensional neutron rates of order $10^9\,\mathrm{s^{-1}}$ and $10^8\,\mathrm{s^{-1}}$. These rates would have to be realized before losses associated with monochromatization, collimation, polarization, beam splitting, coherence selection, and propagation. The $d = 10^{-6}$ m case is purely illustrative, while the denser cases remain optimistic sensitivity benchmarks.

Independently of the available neutron rate, the residual uncertainty in the recurrence condition constitutes a systematic phase floor. As discussed in Section 2.1, a target sensitivity of 10^{-3} rad at the first recurrence requires control of the combined timing and effective-separation uncertainties at the level of approximately 1.6×10^{-4}.

The neutron–mirror-neutron example uses a neutron wavelength $\lambda = 10$ Å, an arm length $l_a = 20$ cm, and magnetic fields $B_a = 0$ and $B_b = 2 \times 10^{-4}$ T. These values are individually closer to existing neutron technologies. The main experimental difficulties are the accuracy of the dynamical-phase cancellation, the stability of the path-length ratio, and magnetic-field control. The Earth's field, represented in Figure 5 by $B_a = 5 \times 10^{-5}$ T, is already non-negligible relative to the applied fields and must be shielded or included in the analysis. The quantities $\epsilon_{nn'}$ and δm are not fixed by the proposal, and the curves in Figure 5 are sensitivity maps rather than predictions based on an established parameter point.

The neutral-meson construction is primarily a phenomenological and data-analysis proposal. It does not require a literal spatial interferometer, and it does not introduce parameters independent of the conventional mixing quantities z and q/p. Its implementation would require reconstructing the complex time-dependent particle and antiparticle amplitudes in flavour-tagged decay analyses. The resulting geometric-phase combinations would then provide rephasing-invariant null tests and consistency observables to be compared with conventional CPT- and CP-violation fits. A quantitative assessment of their relative statistical sensitivity requires a dedicated detector-level analysis and is beyond the scope of the present review.

The accelerated-detector example requires proper accelerations of order 10^{16}–$10^{17}\,\mathrm{m\,s^{-2}}$, depending on the atomic transition. For a ^{87}Rb atom at $a \sim 10^{16}\,\mathrm{m\,s^{-2}}$, the required force is of order 10^{-9} N. No neutral-atom protocol is specified that could apply such an acceleration selectively to one interferometer arm while preserving the assumed hyperfine two-level structure and path coherence. The calculation therefore represents an idealized physically accelerated quantum-field detector benchmark rather than a near-term atom-interferometry proposal. An analogue simulation would require an explicit mapping reproducing the field correlation function along the accelerated worldline; such a construction is not developed here.

The thermometric construction does not require such extreme acceleration, but it relies on accurate reservoir control, sufficiently long coherence times, interferometric phase stability, calibration of the atom–field coupling, and independent knowledge of the reference temperature. The atomic transitions, evolution times, and reference temperatures employed in Figures 7 and 8 should therefore be interpreted as representative theoretical benchmarks inherited from Refs. [64,65].

These limitations do not alter the formal role of geometric phases as probes of weak interactions or quantum-field responses, but they determine whether a given construction represents a present experimental target, a longer-term proposal, or a theoretical proof of principle.

5. Conclusions

In this work, we have reviewed several applications of non-cyclic geometric phases as a common framework to investigate possible signatures of physics beyond the Standard Model and related fundamental effects. The central idea is that weak interactions, mixing mechanisms, or environmental effects can modify the phase evolution of quantum systems, producing contributions that may be accessible through interferometric or oscillation-based measurements.

In the dark-sector context, we discussed two representative examples. First, we reviewed how axion-like particles can mediate an effective spin-dependent interaction between neutrons, leading to a residual interferometric phase once the ordinary magnetic dipole–dipole contribution is canceled modulo 2π. We then considered neutron–mirror-neutron mixing, showing how the mixing with hidden mirror states can generate a geometric phase that vanishes in the absence of ordinary–mirror neutron coupling.

We also reviewed the use of geometric phases in mixed neutral meson systems. In this case, the effective dynamics is governed by a non-Hermitian Hamiltonian, and the biorthonormal formulation allows one to define geometric phases for mesons and antimesons. The phase difference between particle and antiparticle evolution is directly controlled by the CPT-violating parameter z, and it vanishes in the CPT-invariant limit. Geometric phases therefore provide a phase-based diagnostic of CPT symmetry breaking, and can also encode information on CP-violating particle–antiparticle transitions.

Finally, we discussed open quantum systems and their connection with acceleration-induced and thermal effects. For a two-level atom interacting with the electromagnetic

field, the mixed-state geometric phase depends on the trajectory of the atom and on the properties of the surrounding environment. The difference between the geometric phases of accelerated and inertial detectors probes the acceleration-induced quantum-field vacuum response and contains the thermal contribution associated with the Unruh effect.

Overall, these examples show that geometric phases offer a complementary language for identifying subtle effects associated with hidden-sector interactions, discrete-symmetry violation, non-inertial motion, and thermal environments. High-precision interferometric and oscillation-based systems therefore represent promising platforms in which phase-based signatures of new physics and fundamental quantum phenomena may be investigated.

Author Contributions: Conceptualization, A.C., G.P. and R.S.; methodology, A.C., G.P. and R.S.; formal analysis, A.C., G.P. and R.S.; data curation, A.C., G.P. and R.S.; writing—original draft preparation, A.C., G.P. and R.S.; writing—review and editing, A.C., G.P. and R.S.; visualization, A.C., G.P. and R.S. All authors have read and agreed to the published version of the manuscript.

Funding: We acknowledge partialfinancial support from MUR and INFN. A.C. also acknowledges the COST Action CA1511 Cosmology and Astrophysics Network for Theoretical Advances and Training Actions (CANTATA).

Data Availability Statement: The original contributions presented in this study are included in the article. Further inquiries can be directed to the corresponding author(s)

Acknowledgments: The authors have reviewed and edited the output and take full responsibility for the content of this publication.

Conflicts of Interest: The authors declare no conflicts of interest.

References

1. Bilenky, S.M.; Pontecorvo, B. Lepton Mixing and Neutrino Oscillations. *Phys. Rept.* **1978**, *41*, 225–261. [CrossRef]
2. Gribov, V.N.; Pontecorvo, B. Neutrino astronomy and lepton charge. *Phys. Lett. B* **1969**, *28*, 493. [CrossRef]
3. Bilenky, S.M.; Petcov, S.T.; Pontecorvo, B. Lepton Mixing, $\mu \to e + \gamma$ Decay and Neutrino Oscillations. *Phys. Lett. B* **1977**, *67*, 309. [CrossRef]
4. Wolfenstein, L. Neutrino Oscillations in Matter. *Phys. Rev. D* **1978**, *17*, 2369–2374. [CrossRef]
5. Ahmad, Q.R.; Allen, R.C.; Andersen, T.C.; Anglin, J.D.; Barton, J.C.; Beier, E.W.; Bercovitch, M.; Bigu, J.; Biller, S.D.; Black, R.A.; et al. Direct evidence for neutrino flavor transformation from neutral current interactions in the Sudbury Neutrino Observatory. *Phys. Rev. Lett.* **2002**, *89*, 011301. [CrossRef] [PubMed]
6. Schechter, J.; Valle, J.W.F. Neutrino Masses in SU(2) × U(1) Theories. *Phys. Rev. D* **1980**, *22*, 2227. [CrossRef]
7. Aguilar, A.; Auerbach, L.B.; Burman, R.L.; Caldwell, D.O.; Church, E.D.; Cochran, A.K.; Donahue, J.B.; Fazely, A.; Garvey, G.T.; Gunasingha, R.M.; et al. Evidence for neutrino oscillations from the observation of $\bar{\nu}_e$ appearance in a $\bar{\nu}_\mu$ beam. *Phys. Rev. D* **2001**, *64*, 112007. [CrossRef]
8. Ahn, J.K.; Chebotaryov, S.; Choi, J.H.; Choi, S.; Choi, W.; Choi, Y.; Jang, H.I.; Jang, J.S.; Jeon, E.J.; Jeong, I.S.; et al. Observation of Reactor Electron Antineutrino Disappearance in the RENO Experiment. *Phys. Rev. Lett.* **2012**, *108*, 191802. [CrossRef] [PubMed]
9. Apollonio, M.; Baldini, A.; Bemporad, C.; Caffau, E.; Cei, F.; Declais, Y.; de Kerret, H.; Dieterle, B.; Etenko, A.; Foresti, L.; et al. Limits on neutrino oscillations from the CHOOZ experiment. *Phys. Lett. B* **1999**, *466*, 415–430. [CrossRef]
10. Fukuda, Y.; Hayakawa, T.; Ichihara, E.; Inoue, K.; Ishihara, K.; Ishino, H.; Itow, Y.; Kajita, T.; Kameda, J.; Kasuga, S.; et al. Evidence for oscillation of atmospheric neutrinos. *Phys. Rev. Lett.* **1998**, *81*, 1562–1567. [CrossRef]
11. Abe, Y.; Aberle, C.; dos Anjos, J.C.; Barriere, J.C.; Bergevin, M.; Bernstein, A.; Bezerra, T.J.C.; Bezrukhov, L.; Blucher, E.; Bowden, N.S.; et al. Reactor $\bar{\nu}_e$ disappearance in the Double Chooz experiment. *Phys. Rev. D* **2012**, *86*, 052008. [CrossRef]
12. An, F.P.; Bai, J.Z.; Balantekin, A.B.; Band, H.R.; Beavis, D.; Beriguete, W.; Bishai, M.; Blyth, S.; Boddy, K.; Brown, R.L.; et al. Observation of electron-antineutrino disappearance at Daya Bay. *Phys. Rev. Lett.* **2012**, *108*, 171803. [CrossRef] [PubMed]
13. Capolupo, A.; Lambiase, G.; Quaranta, A. Neutrinos in curved spacetime: Particle mixing and flavor oscillations. *Phys. Rev. D* **2020**, *101*, 095022. [CrossRef]
14. Capolupo, A.; De Maria, G.; Monda, S.; Quaranta, A.; Serao, R. Quantum Field Theory of Neutrino Mixing in Spacetimes with Torsion. *Universe* **2024**, *10*, 170. [CrossRef]

15. Capolupo, A.; Monda, S.; Pisacane, G.; Quaranta, A.; Serao, R. Dark Universe from QFT Mechanisms and Possible Experimental Probes. *Universe* **2025**, *11*, 142. [CrossRef]
16. Capolupo, A.; Quaranta, A.; Serao, R. Field Mixing in Curved Spacetime and Dark Matter. *Symmetry* **2023**, *15*, 807. [CrossRef]
17. Capolupo, A.; Quaranta, A.; Serao, R. The impact of the X_{17} boson on particle physics anomalies: Muon anomalous magnetic moment, Lamb shift and *W* mass. *Phys. Dark Univ.* **2025**, *47*, 101748. [CrossRef]
18. Abi, B.; Albahri, T.; Al-Kilani, S.; Allspach, D.; Alonzi, L.P.; Anastasi, A.; Anisenkov, A.; Azfar, F.; Badgley, K.; Baeßler, S.; et al. Measurement of the Positive Muon Anomalous Magnetic Moment to 0.46 ppm. *Phys. Rev. Lett.* **2021**, *126*, 141801. [CrossRef] [PubMed]
19. Bennett, G.W.; Bousquet, B.; Brown, H.N.; Bunce, G.; Carey, R.M.; Cushman, P.; Danby, G.T.; Debevec, P.T.; Deng, H.; Deile, M.; et al. Measurement of the Negative Muon Anomalous Magnetic Moment to 0.7 ppm. *Phys. Rev. Lett.* **2004**, *92*, 161802. [CrossRef] [PubMed]
20. Navarro, J.F.; Frenk, C.S.; White, S.D.M. The Structure of Cold Dark Matter Halos. *Astrophys. J.* **1996**, *462*, 563–575. [CrossRef]
21. Bertone, G.; Hooper, D.; Silk, J. Particle Dark Matter: Evidence, Candidates and Constraints. *Phys. Rep.* **2005**, *405*, 279–390. [CrossRef]
22. Jungman, G.; Kamionkowski, M.; Griest, K. Supersymmetric Dark Matter. *Phys. Rep.* **1996**, *267*, 195–373. [CrossRef]
23. Preskill, J.; Wise, M.B.; Wilczek, F. Cosmology of the Invisible Axion. *Phys. Lett. B* **1983**, *120*, 127–132. [CrossRef]
24. Capozziello, S.; De Laurentis, M. Extended Theories of Gravity. *Phys. Rep.* **2011**, *509*, 167–321. [CrossRef]
25. Chevallier, M.; Polarski, D. Accelerating Universes with Scaling Dark Matter. *Int. J. Mod. Phys. D* **2001**, *10*, 213–223. [CrossRef]
26. Rubin, V.C.; Ford, W.K., Jr. Rotation of the Andromeda Nebula from a Spectroscopic Survey of Emission Regions. *Astrophys. J.* **1970**, *159*, 379–403. [CrossRef]
27. Rubin, V.C.; Ford, W.K., Jr.; Thonnard, N. Rotational Properties of 21 Sc Galaxies with a Large Range of Luminosities and Radii, from NGC 4605 to UGC 2885. *Astrophys. J.* **1980**, *238*, 471–487. [CrossRef]
28. Trimble, V. Existence and Nature of Dark Matter in the Universe. *Annu. Rev. Astron. Astrophys.* **1987**, *25*, 425–472. [CrossRef]
29. Corbelli, E.; Salucci, P. The Extended Rotation Curve and the Dark Matter Halo of M33. *Mon. Not. R. Astron. Soc.* **2000**, *311*, 441–447. [CrossRef]
30. Clesse, S.; García-Bellido, J. Seven Hints for Primordial Black Hole Dark Matter. *Phys. Dark Universe* **2018**, *22*, 137–146. [CrossRef]
31. Salucci, P. The Distribution of Dark Matter in Galaxies. *Astron. Astrophys. Rev.* **2019**, *27*, 2. [CrossRef]
32. Capolupo, A.; Giampaolo, S.M.; Lambiase, G.; Quaranta, A. Probing quantum field theory particle mixing and dark-matter-like effects with Rydberg atoms. *Eur. Phys. J. C* **2020**, *80*, 423. [CrossRef]
33. Capolupo, A.; Capozziello, S.; Pisacane, G.; Quaranta, A. Missing matter in galaxies as a neutrino mixing effect. *Phys. Dark Univ.* **2025**, *48*, 101894. [CrossRef]
34. Capolupo, A.; Pisacane, G.; Quaranta, A.; Serao, R. Single arm interferometry to probe the scalar field dark matter. *Phys. Rev. D* **2026**, *113*, 055027. [CrossRef]
35. Peccei, R.D.; Quinn, H.R. CP Conservation in the Presence of Instantons. *Phys. Rev. Lett.* **1977**, *38*, 1440–1443. [CrossRef]
36. Peccei, R.D.; Quinn, H.R. Constraints Imposed by CP Conservation in the Presence of Instantons. *Phys. Rev. D* **1977**, *16*, 1791–1797. [CrossRef]
37. Weinberg, S. A New Light Boson? *Phys. Rev. Lett.* **1978**, *40*, 223–226. [CrossRef]
38. Wilczek, F. Problem of Strong *P* and *T* Invariance in the Presence of Instantons. *Phys. Rev. Lett.* **1978**, *40*, 279–282. [CrossRef]
39. Raffelt, G.G. Astrophysical methods to constrain axions and other novel particle phenomena. *Phys. Rept.* **1990**, *198*, 1–113. [CrossRef]
40. Capolupo, A.; Lambiase, G.; Quaranta, A.; Giampaolo, S.M. Probing axion mediated fermion–fermion interaction by means of entanglement. *Phys. Lett. B* **2020**, *804*, 135407. [CrossRef]
41. Marsh, D.J.E. Axion Cosmology. *Phys. Rept.* **2016**, *643*, 1–79. [CrossRef]
42. Lee, T.D.; Yang, C.N. Question of Parity Conservation in Weak Interactions. *Phys. Rev.* **1956**, *104*, 254–258. [CrossRef]
43. Kobzarev, I.Y.; Okun, L.B.; Pomeranchuk, I.Y. On the possibility of experimental observation of mirror particles. *Sov. J. Nucl. Phys.* **1966**, *3*, 837–841.
44. Blinnikov, S.I.; Khlopov, M.Y. On possible effects of 'mirror' particles. *Sov. J. Nucl. Phys.* **1982**, *36*, 472.
45. Berezhiani, Z. Mirror world and its cosmological consequences. *Int. J. Mod. Phys. A* **2004**, *19*, 3775–3806. [CrossRef]
46. Hodges, H.M. Mirror baryons as the dark matter. *Phys. Rev. D* **1993**, *47*, 456–459. [CrossRef] [PubMed]
47. Foot, R. Mirror dark matter: Cosmology, galaxy structure and direct detection. *Int. J. Mod. Phys. A* **2014**, *29*, 1430013. [CrossRef]
48. Hostert, M.; McKeen, D.; Pospelov, M.; Raj, N. Dark sectors in neutron-shining-through-a-wall and nuclear-absorption signals. *Phys. Rev. D* **2023**, *107*, 075034. [CrossRef]
49. Berezhiani, Z.; Nesti, F. Supersymmetric SO(10) for fermion masses and mixings: Rank-1 structures of flavor. *JHEP* **2006**, *3*, 041. [CrossRef]

50. Berezhiani, Z.; Bento, L. Neutron–mirror neutron oscillations: How fast might they be? *Phys. Rev. Lett.* **2006**, *96*, 081801. [CrossRef] [PubMed]
51. Belfatto, B.; Berezhiani, Z. How light the lepton flavor changing gauge bosons can be. *Eur. Phys. J. C* **2019**, *79*, 202. [CrossRef]
52. Czarnecki, A.; Marciano, W.J.; Sirlin, A. Neutron Lifetime and Axial Coupling Connection. *Phys. Rev. Lett.* **2018**, *120*, 202002. [CrossRef] [PubMed]
53. Capolupo, A. Probing CPT violation in meson mixing by non-cyclic phase. *Phys. Rev. D* **2011**, *84*, 116002. [CrossRef]
54. Capolupo, A.; Giampaolo, S.M.; Quaranta, A. Testing CPT violation, entanglement and gravitational interactions in particle mixing with trapped ions. *Eur. Phys. J. C* **2021**, *81*, 410. [CrossRef]
55. Capolupo, A.; Pisacane, G.; Quaranta, A.; Romeo, F. Probing mirror neutrons and dark matter through cold neutron interferometry. *Phys. Dark Univ.* **2024**, *46*, 101688. [CrossRef]
56. Werner, S.A.; Staudenmann, J.L.; Colella, R. Effect of earth's rotation on the quantum mechanical phase of the neutron. *Phys. Rev. Lett.* **1979**, *42*, 1103–1106. [CrossRef]
57. Wagh, A.G.; Rakhecha, V.C.; Fischer, P.; Ioffe, A. Neutron Interferometric Observation of Noncyclic Phase. *Phys. Rev. Lett.* **1998**, *81*, 1992–1995. [CrossRef]
58. Allman, B.E.; Kaiser, H.; Werner, S.A.; Wagh, A.G.; Rakhecha, V.C.; Summhammer, J. Observation of Geometric and Dynamical Phases by Neutron Interferometry. *Phys. Rev. A* **1997**, *56*, 4420–4439. [CrossRef]
59. Filipp, S.; Hasegawa, Y.; Loidl, R.; Rauch, H. Noncyclic Geometric Phase Due to Spatial Evolution in a Neutron Interferometer. *Phys. Rev. A* **2005**, *72*, 021602. [CrossRef]
60. Brax, P.; Fichet, S. Scalar-Mediated Quantum Forces between Macroscopic Bodies and Interferometry. *Phys. Dark Universe* **2023**, *42*, 101294. [CrossRef]
61. Pancharatnam, S. Generalized Theory of Interference, and Its Applications. Part I. Coherent Pencils. *Proc. Indian Acad. Sci. Sect. A* **1956**, *44*, 247–262. [CrossRef]
62. Berry, M.V. Quantal Phase Factors Accompanying Adiabatic Changes. *Proc. R. Soc. Lond. Ser. A Math. Phys. Sci.* **1984**, *392*, 45–57. [CrossRef]
63. Mukunda, N.; Simon, R. Quantum Kinematic Approach to the Geometric Phase. I. General Formalism. *Ann. Phys.* **1993**, *228*, 205–268. [CrossRef]
64. Capolupo, A.; Vitiello, G. Probing Hawking and Unruh effects and quantum field theory in curved space by geometric invariants. *Phys. Rev. D* **2013**, *88*, 024027. [CrossRef]
65. Capolupo, A.; Vitiello, G. Vacuum Condensate, Geometric Phase, Unruh Effect, and Temperature Measurement. *Adv. High Energy Phys.* **2015**, *2015*, 878043. [CrossRef]

Disclaimer/Publisher's Note: The statements, opinions and data contained in all publications are solely those of the individual author(s) and contributor(s) and not of MDPI and/or the editor(s). MDPI and/or the editor(s) disclaim responsibility for any injury to people or property resulting from any ideas, methods, instructions or products referred to in the content.